Transition Metal Doped Smart Glass with Pressure and Temperature Sensitive Luminescence

Authors: Shichao Lv,[1] B. Shanmugavelu,[1] Yunpeng Wang,[2] Qiannan Mao,[1] Yujun Zhao,[2] Yongze Yu,[1] Jianhua Hao,[3] Qinyuan Zhang,[1] Jianrong Qiu,[4] and Shifeng Zhou[1]*

Affiliations:

[1]State Key Laboratory of Luminescent Materials and Devices Guangdong Engineering Technology Research and Development Center of Special Optical Fiber Materials and Devices, School of Materials Science and Engineering, South China University of Technology, Guangzhou 510640, China

[2]Department of Physics, South China University of Technology, Guangzhou 510640, China

[3]Department of Applied Physics, The Hong Kong Polytechnic University, Hong Kong, China

[4]College of Optical Science and Engineering, Zhejiang University, Hangzhou 310027, China

The development of future transparent intelligent systems demands smart glass with multifunctional sensing capabilities. Here, the realization of a smart glass with dual temperature and pressure sensing function by using Mn^{2+}-doped nanostructured gallate glass for the first time is reported. The material exhibits exceptional temperature response in the range of 323–523 K and the maximal relative temperature sensitivity reaches as high as 2.51% K^{-1} at 523 K. The material is also sensitive to the pressure fluctuation and displays bright green pressure-induced luminescence. A combination of structural and optical analysis and theoretical calculation reveals that the local dopant orientation in nanodomain inside glass contributes to the previously unrealized sensing behavior. The critical factors governing the sensing performance are identified and the cooperative effects between the local chemical bonding and domain size contribute greatly to the remarkable enhancement of the sensitivity. The results highlight that the precise control over the doping process offers a great opportunity to design new smart glass.

Introduction

Fans of the “A Day Made of Glass” series might be highly encouraged by the future of the glass-based devices with amazing transparent display, health monitoring, and communication applications.[1] Even beyond the realm of fictitious scene, many efforts have currently driven toward this target and, there have been some reports describing the coated glass and composite able to response the surrounding environment changes.[2–7] However, these works are still relied on the use of external functional film coated on the glass. Despite enormous research efforts, the design and synthesis of an inherently smart glass remains a significant challenge.

Our strategy to circumvent above fundamental limitation involves the creation of smart spots in glass via rational doping. We are particularly interested in transition metal ions because of their unique electronic configuration. Impressively, their outermost atomic orbitals are only partly occupied by electrons, which strongly interacts with ligands, neighboring ions and foreign species that bind to the metal.[8] Inspired by this fact, we supposed that the glass can be potentially “intelligentized” if one can rationally anchor transition metal dopants in appropriate sites. Another major challenge for realization of smart glass is the design of appropriate glass host for transition metal doping. As well known, silica glass can only provide distorted tetrahedral position, which is believed to be not appropriate for activation of transition metal dopant. From this view of point, the most promising candidate should be multicomponent glass because it can provide rich tetrahedral, octahedral and even dodecahedral positions for dopants. Furthermore, the multicomponent glass possesses distinguishing kinetic constraints and they can be

controllably released to trigger local ordering for increasing the dopant orientation, which is expected to remarkably enhance the optical activity of the system.[9–11] Guided by this rule, we describe a conceptually new smart glass which can simultaneously report the temperature variations and pressure fluctuations. We find that rational doping can be realized via engineering the relaxation of glass phase. Significantly, controllable segregation of transition metal dopants with precisely defined ligand environment in glass can be achieved. As a result, the reconstructed glass shows temperature dependent luminescence with great sensitivity and interesting strain-induced emission. This work represents the first proof-of-principle demonstration of smart glass with multifunctional sensing properties.

Results and Discussion

Structural and Spectroscopic Properties. Manganese ion (Mn^{2+})-doped gallate glass was chosen as the model system owing to the ability of Mn^{2+} to provide single fingerprint emission band and the benefit of gallate host for producing appropriate crystal field for transition metal dopant.[12,13] Furthermore, the Mn^{2+} dopant acts as not only emitter but also paramagnetic center (S = 5/2), and thus potentially gifting the material system with multiple sensing capacities.[14–16] For efficient activation of the dopant, thermal-treatment was processed for inducing glass relaxation by referring the differential scanning calorimetric analysis (Figure S1, Supporting Information). Based on the thermal analysis results, nanostructured glass samples were prepared by heat-treating the as-made glass at 900, 950, and 1000 °C for 2 h (labeled as NG900, NG950,

and NG1000, respectively). The obtained samples were first examined by X-ray powder diffraction (XRD) and Raman scattering spectroscopy (Figure 1a,b). The XRD patterns of the samples heat-treated above 900 °C exhibit well defined diffraction peaks which can be assigned to the pure $ZnGa_2O_4$ spinel phase (JCPDS no. 38-1240).[17,18] In as-made glass, only broad humps can be observed, indicating the amorphous nature. Raman scattering spectra also clearly show the fingerprint vibration bands of the ordered structural units in nanostructured glass samples. The sharp peaks at 606 and 713 cm^{-1} can be well attributed to the T_{2g} mode and A_{1g} vibrations of regular -Zn-O-Ga-O- bonding, further confirming the formation of $ZnGa_2O_4$ crystalline phase.[19]

A representative transmission electron microscopy (TEM) image of the NG1000 sample reveals the presence of monodispersed nanocrystals (≈40 nm) inside the glass matrix. High-resolution TEM (HRTEM) image of a single particle exhibits clear lattice fringes of the (111) plane of $ZnGa_2O_4$ spinel phase with the d-spacing of ≈0.48 nm. High-angle annular dark-field image and the corresponding energy dispersive X-ray spectroscopic (EDS) maps and line profiles of Mn in NG1000 sample (Figures S2 and S3, Supporting Information) clearly show that Zn, Ga, Mn, and Si elements are homogeneously distributed and there are no obvious difference between Zn and Ga, indicating the excellent crystallinity of $ZnGa_2O_4$ spinel phase. The results show that the distribution of Mn element is well consistent with Zn and Ga and mainly enriches in the crystalline phase, suggesting that Mn^{2+} ions are selectively incorporated into the $ZnGa_2O_4$ nanocrystalline phase (Figures S2 and S3, Supporting Information). The atomic ratio of Zn/Ga is estimated to be nearly 1:2 (Figure S4, Supporting Information),

97 further confirming the stoichiometric composition of the $ZnGa_2O_4$ phase. The atomic
98 ratio of Mn/Zn in $ZnGa_2O_4$ spinel phase is estimated to be nearly 0.93:100 (Figure S4,
99 Supporting Information). The lattice constant and primitive cell volume of NG1000
100 samples were also been characterized (Figures S5 and S6, Supporting Information). It
101 can be observed that the lattice constant and cell volume increase coincidentally with
102 the enhancement of the Mn^{2+} concentration. The lattice constant of $ZnGa_2O_4$ and
103 $MnGa_2O_4$ crystal is 8.3354 and 8.4577 Å, respectively. Above results demonstrate that
104 Mn^{2+} ions occupy the Zn^{2+} ions in NG1000 sample.
105 Experimental results show that glass relaxation is critical for activation of Mn^{2+} dopant
106 in glass. Notably, the in-situ precipitation of the $ZnGa_2O_4$ crystalline phase inside glass
107 dramatically changes the emission color from red to green (the inset of Figure 2a).
108 Photoluminescence studies (Figure 2a) indicate that as-made glass shows a single broad
109 excitation band at 304 nm and emission band at 635 nm, which can be ascribed to the
110 $O^{2-} - Mn^{2+}$ charge transfer transition and $^4T_1(^4G) \rightarrow {}^6A_1(^6S)$ transitions of Mn^{2+}
111 dopant.[20] In stark contrast, the nanostructured glass samples exhibits several sharp
112 excitation peaks at 360, 383, 426, and 450 nm and a much narrow emission band at 506
113 nm, which can be ascribed to the $^6A_1 \rightarrow {}^4E(^4D)$ $^6A_1 \rightarrow {}^4D(T_{2g})$, $^6A_1 \rightarrow [{}^4G(E_g)$, $^4G(A_{1g}]$,
114 $^6A_1 \rightarrow {}^4G(^4T_{2g})$, and $^4T_1(^4G) \rightarrow {}^6A_1(^6S)$ electronic transitions, respectively.[20–25] The
115 drastic decrease in the spectral broadening and appearance of sharp fingerprint peaks is
116 probably originated from the selective incorporation of Mn^{2+} inside the nanocrystalline
117 phase, thus indicating the occurrence of collective orientation of dopant during glass
118 relaxation. Electron paramagnetic resonance (EPR) spectroscopy was employed to

further clarify the exact chemical environment around Mn^{2+} dopant and the results are shown in Figure 2b. In as-made glass sample, the EPR signal is mainly originated from the Mn^{2+} ions in octahedral sites. In contrast, in the case of NG1000 sample, the EPR signal associated with Mn^{2+} ions in tetrahedral sites drastically increases while the signal originated from Mn^{2+} ions in octahedral sites decreases. This indicates that when the $ZnGa_2O_4$ crystalline phase precipitates inside the glass, most of the Mn^{2+} ions occupy tetrahedral position and most probably, they substitute for Zn^{2+} ions which are coordinated by four oxygen ions.

As a typical transition metal dopant, the hallmark of Mn^{2+} ions is that the electrons in their outmost d orbital strongly interact with their ligands. Thus, their optical response feature can be further discussed by studying the symmetry of impurity ion sites and the covalency of local chemical bonding, which can be described by the crystal field strength D*q* and the Racah parameter B, respectively. These two parameters can be calculated from Tanabe–Sugano (T–S) matrices with trees correction,[26] as described in the following equations

$$^6A_1(^6S) \rightarrow {}^4A_1, {}^4E\,(^4G) = 10B + 5C + 20\alpha \quad (1)$$

$$^6A_1(^6S) \rightarrow {}^4E\,(^4D) = 17B + 5C + 6\alpha \quad (2)$$

$$^6A_1(^6S) \rightarrow {}^4T_2\,(^4D) = 13B + 5C + 8\alpha \quad (3)$$

$$^6A_1(^6S) \rightarrow {}^4T_2\,(^4G) = -10Dq + 18B + 6C - (26B^2/10Dq) + 22\alpha \quad (4)$$

where α is the trees correction parameter. Based on the characteristic electronic transitions obtained from the excitation spectra of Mn^{2+} (Figure 2a), the values of Dq,

B, and α were estimated to be 963, 755, and 81 cm^{-1} for Mn^{2+} in as-made glass, and 861, 740, and 64 cm^{-1} for Mn^{2+} in NG1000, respectively. Accordingly, we indicate the corresponding energy-level configuration of Mn^{2+} in the Tanabe–Sugano diagram (Figure 2c) and, typically, it presents notable shift to the low crystal field strength region after glass relaxation. The results give firm evidence that Mn^{2+} dopants are selectively incorporated into the low coordination sites. The phenomenon of luminescence color change can also be understood from the obtained energy-level configuration. As shown in Figure 2c, the decrease of crystal field strength resulted from the collective orientation of Mn^{2+} may shift the vertical positions of the energy levels, leading to a notable change of the energy gap between the $^4T_1(^4G)$ and $^6A_1(^6S)$ levels. Significantly, the activation efficiency of Mn^{2+} dopant in nanostructured glass through glass relaxation was estimated to be larger than 95%, which is believed to be much higher than the nanostructures fabricated via solution method due to the frequently observed "intrinsic self-purification" process in solution doping process.[27] Benefited from the high activation efficiency of dopant, the fabricated sample presents intense luminescence and it can still be clearly observed by naked eye even in tiny fibers (≈100 μm) (Figure 2a). Moreover, the sample shows strong green long-lasting luminescence when it is excited by UV light (Figure S7, Supporting Information).

To shed more light on the electronic structures of Mn^{2+}-doped $ZnGa_2O_4$ phase, the first-principles calculations are performed based on the density functional theory (DFT). Figure 3a,b shows the calculated electronic band dispersion and partial densities of states (PDOS) of the perfect $ZnGa_2O_4$. The results clearly indicate that $ZnGa_2O_4$ is a

semiconductor with the computed band gap (HSE) of 4.45 eV, which is consistent with the computed and experimental value.[28] The stable chemical potential region of Mn^{2+}-doped $ZnGa_2O_4$ is calculated, as shown in Figure 3c. It can be found that the stable region (in orange color) is relatively small. The computed PDOS of $ZnGa_2O_4$ after incorporation of Mn is also presented in Figure 3d. The Mn^{2+} dopant externally introduce defect levels which are mainly contributed from Mn^{2+}-3*d* levels. Our calculations show that doping of Mn^{2+} inside the $ZnGa_2O_4$ host results in a notable splitting of its 3*d* levels. Furthermore, the calculated formation energy of MnZn is smaller than that of MnGa. Our calculations are well consistent with the experimental observations demonstrating that Mn^{2+} dopant can be rationally activated through controllable relaxation in the nanostructured glass.

Temperature and Pressure Sensitive Luminescence. Given the strong Mn^{2+}-ligand coupling and the high activation efficiency of dopant, we examined the capacity of Mn^{2+}-doped nanostructured glass for sensing temperature change. Mn^{2+}-doped nanostructured glass can be drawn into fiber and connected to the commercial silica fiber for temperature sensing purpose (Figure 4a). We have employed luminescence lifetime mode for this purpose since luminescent thermometers are noncontact and can operate in the remote condition. The set-up for the measurement of temperature dependent luminescence and decay is given in the Figure 4a. The measured luminescence spectra in the range of 323–523 K for NG1000 sample is shown in Figure 4b. It can be observed that the luminescence intensity decreases notably with increasing temperature, indicating the high potential sensitivity. The temperature dependent

luminescence decay curves of the same sample are shown in Figure 4c. The decay curves can be well fitted to the second order exponential equation

$$I(t) = A_1 \exp(-t/\tau_1) + A_2 \exp(-t/\tau_2) \quad (5)$$

where *I* is the luminescence intensity, t is the time, A_1 and A_2 are constants, τ_1 and τ_2 are short and long parts of lifetime. The average lifetimes can be calculated from the following formula

$$\tau = \left(A_1\tau_1^2 + A_2\tau_2^2\right)/\left(A_1\tau_1 + A_2\tau_2\right) \quad (6)$$

The lifetime of the NG1000 sample dramatically decreases with increasing temperature and the temperature dependent lifetime values are shown in Figure 4d.

The critical parameter that makes doped materials relevant for temperature sensing applications is sensitivity (S), which can be calculated by the following equation

$$S = \left|\frac{1}{\tau}\frac{d\tau}{dT}\right| \quad (7)$$

The results are shown in Figure 4d and it can be clearly seen that the relative sensitivity remarkably increases with enhancement of temperature. The maximal relative sensitivity is found to be 2.51% K^{-1} at 523 K. We summarized the sensitivity of some sensing materials based on the same lifetime mode, as shown in Table 1. It is exciting that the sensitivity is superior to that of the other doped material system.[29–33]

The temperature sensitivity of the materials is decided by many factors such as energy separation between thermally coupled levels, radiative transition probabilities, which in turn depends upon the local chemistry around the dopant. First, the nature of intrinsic

chemical bond is one of the important factor and it has been found that temperature sensitivity of the material is directly proportional to the bond covalency.[34] Hence, the increase in the covalency of the system may potentially lead to the enhancement of the sensitivity. The degree of covalency in transition metal activated materials is determined by the parameter called nephelauxetic ratio β = B (Racah parameter in complex)/B_0 (Racah parameter in free ion). Generally, the decrease in the value of β increases the covalency of the materials due to the suppressed interelectronic repulsion. In the present work, β was calculated by keeping the B_0 value as 960 cm^{-1} for Mn^{2+} ion and the value of β is found to be 0.7708 for the NG1000 sample. A comparison of β value for different material systems is given Table 1. It can be found that β value of the obtained nanostructured glass is smaller than previously reported material systems except for Cr^{3+}-doped $ZnGa_2O_4$. The results indicate that the high bond covalency of Mn-O in nanostructured gallate glass greatly contributes to the observed superior temperature sensitivity.

Another important parameter that influences the temperature sensitivity of the system is the extrinsic nonradiative relaxation channels. Especially in the case of nanothermometer with reduced physical dimension, the concentration of surface dopant ions increases and the fluorescence from these ions should be remarkably influenced by the nonradiative relaxation process due to residual hydroxyl ions, surface defects and other impurities.[35,36] To study this factor, the size of nanodomain obtained from TEM results in the present work have been compared with the other previously reported lifetime based temperature sensing systems. As shown in Table 1, it can be found that

the size of nanodomain of the present work is higher than the other systems. This indicates that the present system has lesser nonradiative relation rate than other systems, which in turn led to the increased temperature sensitivity. Importantly, the temperature sensitivity follows a systematic trend with the size of nanocrystals. It can be used to explain the case in Cr^{3+} doped $ZnGa_2O_4$ system which shows lower β value while less temperature sensitivity: the physical size of $ZnGa_2O_4$ nanostructure is much smaller compared with that of the nanodomain in the present work; it might lead to the higher nonradiative relation rate in the former material system and smaller temperature sensitivity. According to the Raleigh–Gans–Debye theory,[37] the increase of crystal size beyond certain limit (above ≈70 nm) leads to maximum light scattering and affects the transparency. Thus, a perfect balance has to be maintained between the crystallite size and transparency of material in order to achieve higher sensitivity in fiber detector. Significantly, we also found that Mn^{2+}-doped nanostructured glass can be used for indicating the pressure fluctuation. In a typical experiment, the sample (NG1000) was irradiated with 254 nm UV lamp for 5 min. After switching of the UV lamp, the sample shows bright green afterglow luminescence and the luminescence intensity gradually decrease. After 10 min, the afterglow luminescence cannot be clearly observed with the naked eye and the corresponding photograph is shown in Figure 5a. Interestingly, the sample emits bright green luminescence again when it was exerted with an outward shock pressure (Figure 5b). The pressure-induced luminescence was measured and the result is shown in Figure 5c. It can be observed that the corresponding spectrum is completely consistent with the luminescence of Mn2+ in the nanostructured sample.

Notably, as-made glass sample does not show any pressure-induced luminescence. Thus, the observed pressure-induced luminescence should be associated with the selective incorporation of Mn^{2+} in nanocrystalline phase in nanostructured glass.

The origin of the observed pressure-induced luminescence in nanostructured sample might be associated with the external field dependent electron and/or hole releasing, which is mainly governed by the carrier traps. As well known, $ZnGa_2O_4$ nanodomain precipitated from glassy phase owns unique structure. It belongs to spinel compound having the formula of AB_2O_4 in which most of Zn^{2+} and Ga^{3+} ions occupy tetrahedral A and octahedral B sites, respectively. Importantly, it is characterized by the coexistence of structure inversion: part of Zn^{2+} ions occupy the octahedral (B) sites and Ga^{3+} ions occupy tetrahedral (A) sites. This site exchange of cations creates the point/lattice defects with different charges in the host matrix and these defects are called as antisite defects. Furthermore, the tetrahedral and octahedral site defects associated with the Ga^{3+} and Zn^{2+} ions and rich oxygen vacancies may also act as carrier traps for electrons and holes respectively.

To clarify the dominated defects, we performed calculations on the formation energies ($\Delta H^{\alpha,q}(\mu_i, E_F)$) of various defects according to the formula

$$\Delta H^{\alpha,q}(\mu_i, E_F) = \Delta H^{\alpha,q}(0,0) + \sum_i n_i \mu_i + qE_F \qquad (8)$$

where a defect α is ionized to the charge state q, μ_i is the chemical potential of the component elements, E_F is the Fermi energy, $\Delta H^{\alpha,q}(0, 0)$ is the formation energy when $\mu_i = 0$ and $E_F = 0$, μ_i (q) is the number of removed element i when form the defect α in the charge state *q*. As an example, $n_{Ga} = -1$, $n_{Zn} = +1$, and $q = +1$ when the antisite

defect Ga_{Zn}^{+1} is formed. Three extreme cases (O-poor, O-medium, and O-rich) are calculated for various possible defects, including Ga_{Zn}, V_O, O_{Ga}, O_i, O_{Zn}, V_{Ga}, Zn_{Ga}, and V_{Zn}. We mainly focus on the O-poor condition because this case is more close to the experimental condition and the formation of other Mn–O related competitive phase can also be well prevented. Additionally, VO with different charge states is also studied since the removement of one O atom leads to the formation of two unpaired electrons which can be easily ionized. As shown in Figure 6a–d, it can be found that Ga_{Zn}, V_O, V_{Zn}, and Zn_{Ga} show relatively low formation energies.

The contributions of various defects to the optical properties can be discussed based on the trap depth, which is mainly dependent on their transition energy levels. The transition energy levels of various defects with different charge states were calculated and plotted relative to the valence and conduction band edges (Figure 6e). Taking into account the stability of various defects (Figure 6a–d), it can be concluded that V_O should be the dominate defect in the investigated system. The thermodynamic transition levels of V_O are located at 0.86 and 0.93 eV, respectively. To support the theoretical simulations, thermoluminescence measurements were performed and the trap depths and distributions can be obtained by fitting glow curve (Figure S8, Supporting Information). The experimental trap depths are 0.78 and 0.89 eV, which correspond to the simulated shallow and deep traps, respectively.

Based on the above theoretical and experimental analysis, a schematic drawing was used for explaining the possible mechanism of pressure sensitive luminescence. As illustrated in Figure 7, the fluctuation of pressure may potentially leads to the

redistribution of carriers around the defect. Especially, when stress is applied to the Mn^{2+} doped nanostructured glass samples, the local electric-field is created around the nanodomain region due to the triboelectrification process.[38,39] The induced electric field tilts the conduction and valence bands of $ZnGa_2O_4$, which leads to the lowering of bottom of the conduction band. Consequently, the electrons trapped in the defect states are detrapped and released into the conduction band. Thereafter, a recombination occurs between the excited electrons and the trapped holes through the nonradiative process and the energy released in this process is transferred to the Mn^{2+} ions. Subsequently, Mn^{2+} ions are excited into the higher level and then emit green luminescence associated with $T_1(^4G) \rightarrow {}^6A_1(^6S)$ transition during their de-excitation. This is well consistent with the fact that the observed pressure-induced luminescence shows spectrum remarkably similar to that of the photoluminescence (Figure 5c).

Repeatability/reproducibility is an important parameter for the pressure sensing candidate. We tested it by repeating this experiment for many times and the corresponding photographs of pressure-induced luminescence are shown in Figure 8. It can be found that the pressure-induced luminescence produced in this material is highly reproducible, indicating the potential application of the material in nondestructive and reliable pressure or touch sensor. Furthermore, it can be potentially explored to indicate the breaking process of bulk glass, which is critically important for studying the mechanical response of glass materials.

Anticounterfeiting and Secure Communications. Humans have always been fascinated by the art of hiding information like steganography. Writing secret messages

or patterns to prevent the information from visual observation and retrieving the actual content at appropriate moment is an important task in anticounterfeiting and secure communications. Encouragingly, we found that the fabricated NG1000 sample can be potentially used for this purpose. To demonstrate this process, the snake-like pattern has been carved inside the glass by using laser (Figure 9a). The sample was exposed to UV light for one minute and then the excitation light was turned off. When applying a shock pressure, the pattern can be clearly observed (Figure 9b). Furthermore, the covert message such as 2D code and image can be well delivered by combining the afterglow and shock-pressure enhanced luminescence (Figure 9c,d). In contrast to the conventional intelligent media reliant on metastable nanoparticle inks and photochromic molecules,[40–42] our approach provides a multitude of advantages, including much reduced background noise, high security and negligible photobleaching. It should be further noted that the constructed smart glass shows thermal stability up to 650 °C (Figure S1, Supporting Information), indicating its virtually unlimited service lifetime.

Conclusion

Smart glass with temperature- and pressure-sensing functions have been demonstrated in the Mn^{2+}-doped $ZnGa_2O_4$ nanostructured glass. The maximal relative temperature sensitivity for the glass is found to be 2.51% K^{-1} at 523 K, which is higher than those of previously reported systems with lifetime approach. The observed high sensitivity can be attributed to the strong covalency and optimum crystallite size of the

nanostructured system, which ensures the reduced nonradiative relaxation rate and enhanced efficiency. In addition, pressure-induced bright green luminescence has been observed in the sample due to the triboelectric effect. The excellent temperature- and pressure-sensing performance of the constructed material suggests that it may find prospective applications in remote thermometry, real-time pressure monitoring, anticounterfeiting and secure communications. Furthermore, the findings reveal that the basic understanding of bonding nature and rational engineering of structure relaxation of noncrystalline solid is critical for functionalization of glass.

Experimental Section

Preparation: Glass with the composition of $55SiO_2–5Na_2O–16.9ZnO–23Ga_2O_3–0.1MnO$ (in mol%) were prepared by melt-quenching technique using analar grade SiO_2, Na_2CO_3, ZnO, Ga_2O_3, and $MnCO_3$ chemicals. The mixtures of composition were melted in a platinum crucible at about 1600 °C for 1 h and then the melt was quenched on the preheated stainless-steel plates. The prepared glass samples were annealed at 550 °C for 3 h to remove the thermal stress. The samples were then cut, ground and finally polished to a thickness of 1 mm to make them suitable for optical measurements. In order to check the fiber-drawing ability of this material, the glass fiber was fabricated by manual pulling process. In this process, the glass was melted again, and the temperature slowly decreased until the viscosity of the melt became appropriate for pulling glass fibers manually. The diameter and length of the produced glass fiber is found to be 100 μm and 3 m.

Characterization Methods: Differential scanning calorimetry (DSC) experiments were performed on powdered specimens under Argon gas atmosphere at the heating rate of 10 °C min^{-1} using STA449C Jupiter (Netzsch, Bavaria, Germany). The X-ray diffraction measurements of the samples were carried out on a PANalytical (Almelo, the Netherlands) X- ray diffractometer with Cu Kα radiation (λ = 1.5406 Å) at room temperature. The nanostructure and the elemental composition of the samples was examined through transmission electron microscope (TEM), high-resolution transmission electron microscope (HRTEM), scanning transmission electron microscope (STEM) with a high-angle annular dark-field (HAADF) detector and energy dispersive X-ray spectroscopy (EDS) using FEI Tecnai G^2 F20 S-TWIN system (FEI company, USA). The Raman spectra of samples were recorded using Renishaw inVia Raman spectrometer. Electron paramagnetic resonance (EPR) spectra were recorded with an X-band spectrometer (ELEXSYS, Bruker). The excitation and emission spectra and decay curves from room temperature to 523 K were recorded on an FLS920 spectrofluorometer (Edinburgh Instruments). A Xenon Xe900 lamp and a μF900 microsecond flash lamp were used as excitation sources for the steady-state and decay curves measurements respectively. Pressure-induced luminescence signals were measured using the Ocean Optics fiber spectrometer. The photographs of the samples with/without pressure were captured by Canon 5D4 camera in long exposure mode.

ACKNOWLEDGMENTS

S.L. and B.S. contributed equally to this work. The authors gratefully acknowledge

financial support from the National Natural Science Foundation of China (Grant 11474102), the National Science Fund for Excellent Young Scholars of China (Grant 51622206), Fundamental Research Funds for the Central University, the Tip-Top Scientific and Technological Innovative Youth Talents of Guangdong Special Support Program (Grant 2015TQ01C362), and Open Fund of State Key Laboratory of Information Photonics and Optical Communications (Beijing University of Posts and Telecommunications), P. R. China (IPOC2016B003).

REFERENCES

1 Corning, A Day Made of Glass, http://www.corning.com/worldwide/en/innovation/a-day-made-of-glass.html, (accessed: May 2013).

2 J. Hiller, J. D. Mendelsohn, M. F. Rubner, Nat. Mater. 2002, 1, 59.

3 A. Kirihara, K. I. Uchida, Y. Kajiwara, M. Ishida, Y. Nakamura, T. Manak, E. Saitoh, S. Yorozu, Nat. Mater. 2012, 11, 686.

4 A. Llordes, G. Garcia, J. Gazquez, D. J. Milliron, Nature 2013, 15, 323.

5 Y. Yao, K.-T. Lee, X. Sheng, N. A. Batara, N. Hong, J. He, L. Xu, M. M. Hussain, H. A. Atwater, N. S. Lewis, R. G. Nuzzo, J. A. Rogers, Adv. Energy Mater. 2017, 7, 1601992.

6 X.-D. Chen, Z. Chen, W.-S. Jiang, C. Zhang, J. Sun, H. Wang, W. Xin, L. Lin, M. K. Priydarshi, H. Yang, Z.-B. Liu, J.-G. Tian, Y. Zhang, Y. Zhang, Z. Liu, Adv. Mater. 2017, 29, 1603428.

7 M. Dubernet, Y. Gueguen, P. Houizot, F. Célarié, J. C. Sangleboeuf, H. Orain,

T. Rouxel, Appl. Phys. Lett. 2015, 107, 151906.

8 M. A. Hayward, M. J. Rosseinsky, Nature 2007, 450, 960.

9 S. Zhou, Q. Guo, H. Inoue, Q. Ye, A. Masuno, B. Zheng, Y. Yu, J. Qiu, Adv. Mater. 2014, 26, 7966.

10 Y. Yu, Z. Fang, C. Ma, H. Inoue, G. Yang, S. Zheng, D. Chen, Z. Yang, A. Masuno, J. Orava, S. Zhou, J. Qiu, NPG Asia Mater. 2016, 8, e318.

11 M. Micoulaut, Y. Yue, MRS Bull. 2017, 42, 18.

12 Z. Pan, Y.-Y. Lu, F. Liu, Nat. Mater. 2012, 11, 58.

13 X. Liu, Y. Wang, X. Li, Z. Yi, R. Deng, L. Liang, X. Xie, T. B. L. Daniel, S. Song, D. Fan, H. Angelo, H. Zhang, L. Huang, X. Liu, Nat. Commun. 2017, 8, 899.

14 R. Beaulac, P. I. Archer, S. T. Ochsenbein, D. R. Gamelin, Adv. Funct. Mater. 2008, 18, 3873.

15 E. J. McLaurin, V. A. Vlaskin, D. R. Gamelin, J. Am. Chem. Soc. 2011, 133, 14978.

16 X. Wang, M. Que, M. Chen, X. Han, X. Li, C. Pan, Z. Wang, Adv. Mater. 2017, 29, 1605817.

17 G. G. P. Van Gorkom, J. H. Haanstra, H. v. d. Boom, J. Raman Spectrosc. 1973, 1, 513.

18 M. Allix, S. Chenu, E. Véron, T. Poumeyrol, E. A. KouadriBoudjelthia, S. Alahrache, F. Porcher, D. Massiot, F. Fayon, Chem. Mater. 2013, 25, 1600.

19 H. Akazawa, H. Shinojima, J. Phys. Chem. Solids 2018, 117, 60.

20 L. E. Orgel, J. Chem. Phys. 1955, 23, 1004.

21 L. E. Shea, R. K. Datta, J. J. Brown Jr., J. Electrochem. Soc. 1994, 141, 1950.

22 M. Flynn, A. H. Kitai, J. Electrochem. Soc. 2001, 148, H149.

23 G. Anoop, K. M. Krishna, M. K. Jayaraj, J. Electrochem. Soc. 2011, 158, J269.

24 J. S. Kim, H. L. Park, G. C. Kim, T. W. Kim, Y. H. Hwang, H. K. Kim, S. I. Mho, S. D. Han, Solid State Commun. 2003, 126, 515.

25 K. Somasundaram, K. P. Abhilash, V. Sudarsan, P. C. Selvin, R. M. Kadam, Physica B 2016, 491, 79.

26 A. K. Mehra, J. Chem. Phys. 1968, 48, 4384.

27 S. C. Erwin, L. Zu, M. I. Haftel, A. L. Efros, T. A. Kennedy, D. J. Norris, Nature 2005, 436, 91.

28 H. Dixit, N. Tandon, S. Cottenier, R. Saniz, D. Lamoen, B. Partoens, V. Van Speybroeck, M. Waroquier, New J. Phys. 2011, 13, 063002.

29 D. Chen, Z. Wan, Y. Zhou, Z. Ji, J. Eur. Ceram. Soc. 2015, 35, 4211.

30 D. Chen, Z. Wan, Y. Zhou, X. Zhou, Y. Yu, J. Zhong, M. Ding, Z. Ji, ACS Appl. Mater. Interfaces 2015, 7, 19484.

31 X. Li, G. Jiang, S. Zhou, X. Wei, Y. Chen, C. Duan, M. Yin, Sens. Actuators B 2014, 202, 1065.

32 D. Chen, Z. Wan, Y. Zhou, Opt. Lett. 2015, 40, 3607.

33 V. Lojpur, M. G. Nikolic, D. Jovanovic, M. Medic, Z. Antic, M. D. Dramicanin, Appl. Phys. Lett. 2013, 103, 141912.

34 S. F. León-Luis, U. R. Rodríguez-Mendoza, P. Haro-González, I. R. Martín, V.

Lavín, Sens. Actuators B 2012, 174, 176.

35 M. A. R. C. Alencar, G. S. Maciel, C. B. de Araujo, A. Patra, Appl. Phys. Lett. 2004, 84, 4753.

36 F. Wang, J. Wang, X. Liu, Angew. Chem., Int. Ed. 2010, 49, 7456.

37 R. Apetz, M. P. B. van Bruggen, J. Am. Ceram. Soc. 2003, 86, 480.

38 H. Matsui, C.-N. Xu, M. Akiyama, T. Watanabe, Jpn. J. Appl. Phys. 2000, 39, 6582.

39 H. Matsui, C.-N. Xu, Y. Liu, H. Tateyama, Phys. Rev. B 2004, 69, 235109.

40 R. Klajn, P. J. Wesson, K. J. M. Bishop, B. A. Grzybowski, Angew. Chem., Int. Ed. 2009, 48, 1.

41 W. Jeong, M. I. Khazi, D.-H. Park, Y.-S. Jung, J.-M. Kim, Adv. Funct. Mater. 2016, 26, 5230.

42 H. Wu, Y. Chen, Y. Liu, Adv. Mater. 2017, 29, 1605271.

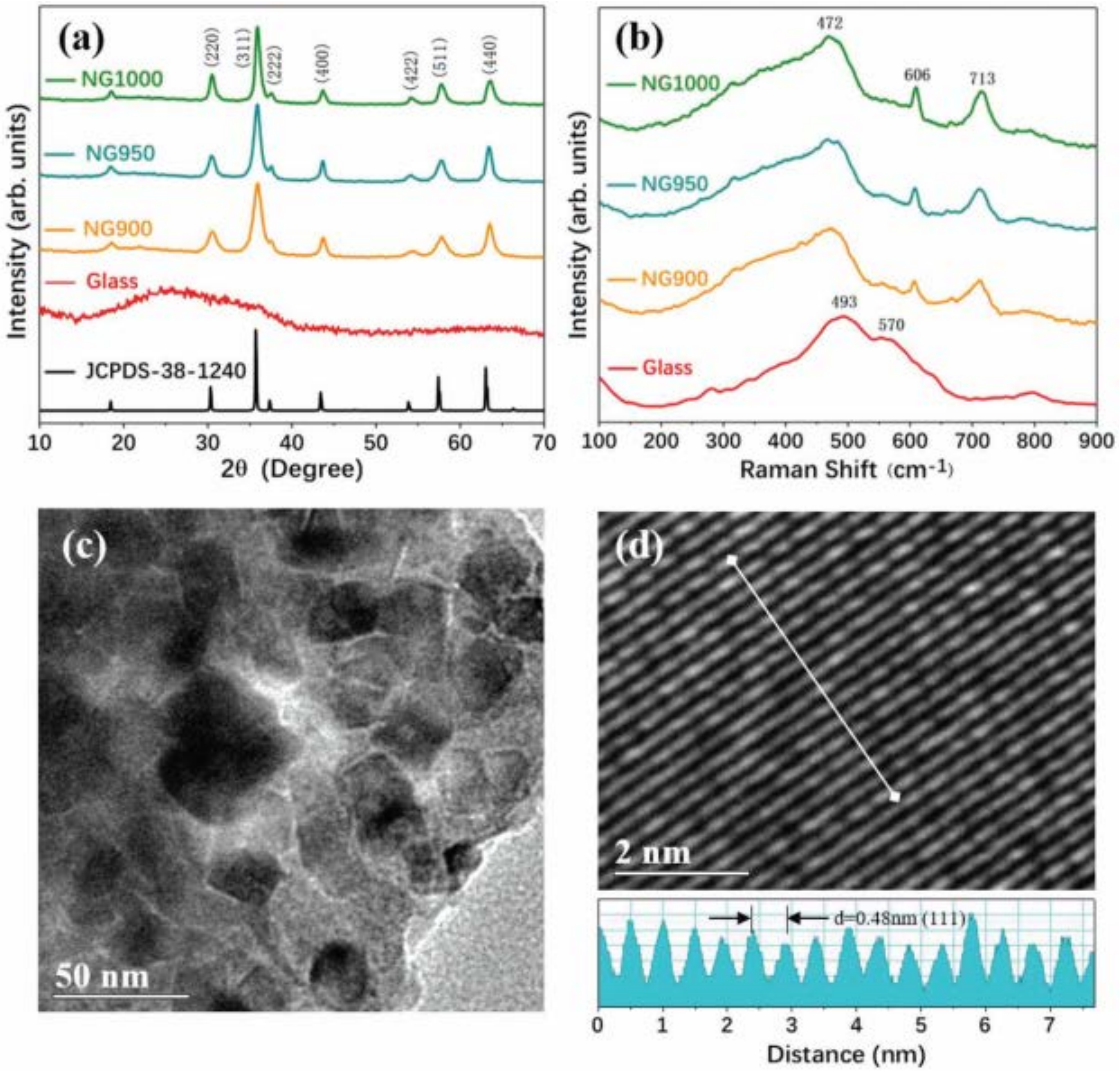

457

458 **Figure 1.** Structural characterizations of the constructed samples. a,b) XRD and Raman

459 patterns of the samples. c,d) TEM and HRTEM images of the NG1000 sample.

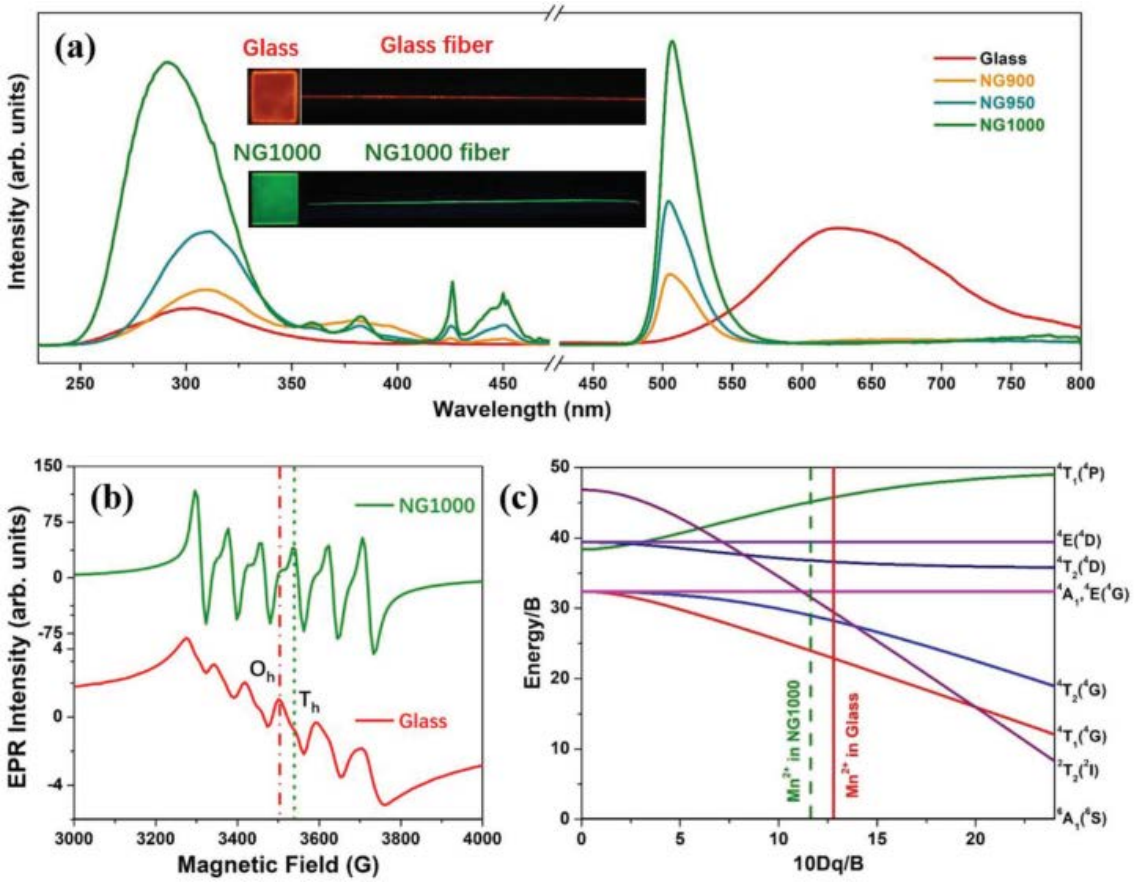

Figure 2. Optical characterizations of the constructed samples. a) Photoluminescence excitation and emission spectra of the samples. In excitation spectra, the monitoring wavelength is 635 nm for glass and 506 nm for the nanostructured glass. In emission spectra, the peak wavelength in the excitation spectrum is chosen as the excitation wavelength. The inset shows the photographs of glass, NG1000 sample and the corresponding fibers. b) EPR spectra of the glass and NG1000 sample. c) Tanabe–Sugano diagram of the glass and NG1000 sample.

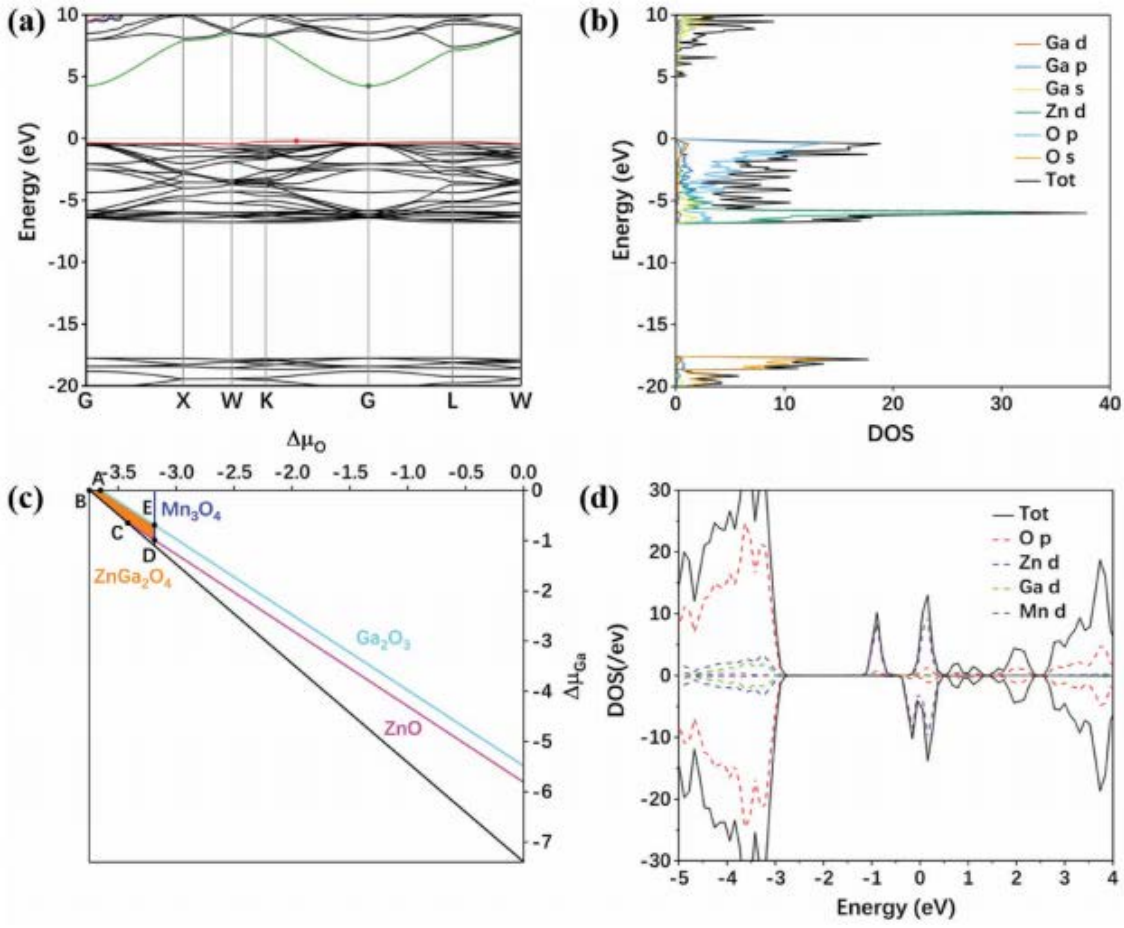

468

469 **Figure 3.** Electronic structures and stability of the precipitated Mn^{2+}-doped $ZnGa_2O_4$

470 phase in the nanostructured glass. a,b) Computed electronic band dispersion and PDOS

471 of $ZnGa_2O_4$. c) Computed chemical potential region which defines the thermodynamic

472 stability of Mn^{2+}-doped $ZnGa_2O_4$. d) Computed PDOS of $ZnGa_2O_4$ after incorporation

473 of Mn. The Fermi level is set to 0 eV.

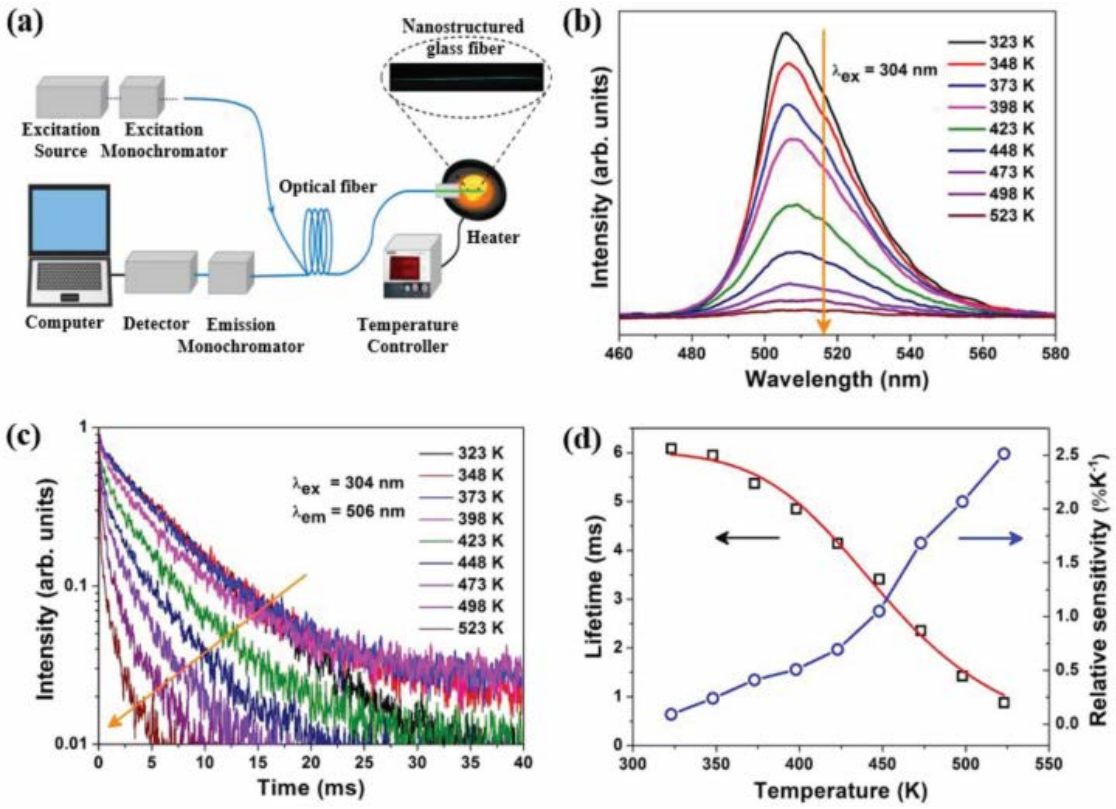

Figure 4. Temperature sensing properties of the nanostructured glass. a) Set-up for temperature sensing measurements. b) Temperature dependent luminescence spectra of the NG1000 sample. c) Temperature dependent decay curves of the NG1000 sample. d) Lifetime and relative sensitivity values of the NG1000 sample.

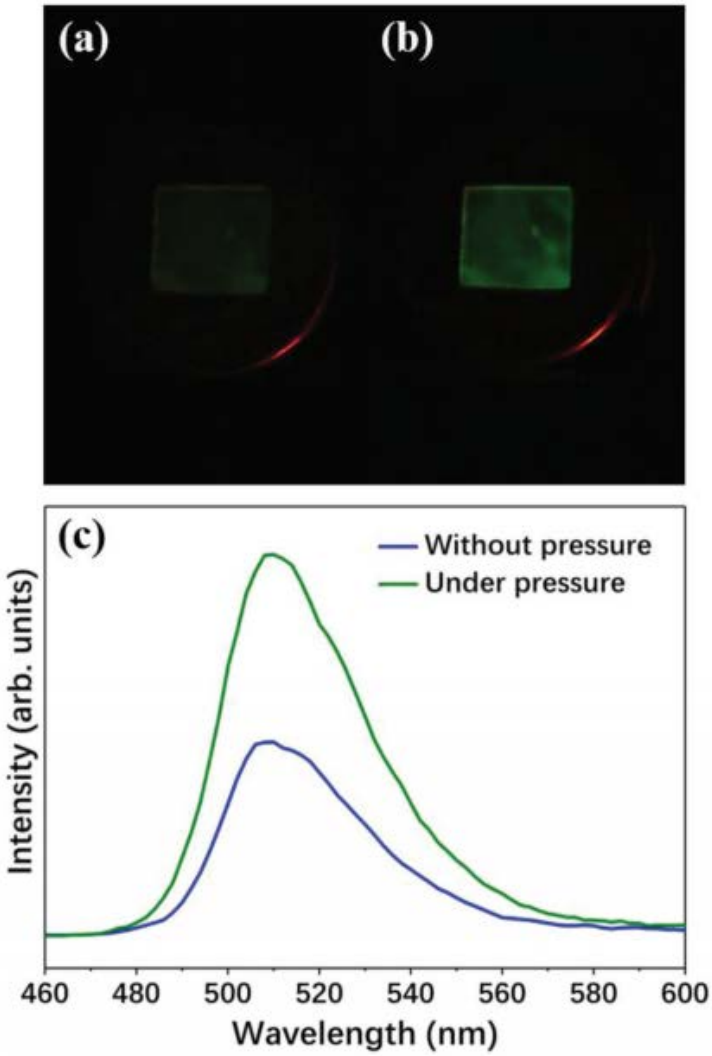

Figure 5. Pressure sensing luminescence of the nanostructured glass. a) Photograph of the NG1000 sample captured after 10 min of switching off UV lamp in the dark environment. Only very weak luminescence can be observed with naked eye. b) Photograph of the NG1000 sample captured when the sample was exerted with a shock pressure. c) The luminescence spectra before and after applying pressure.

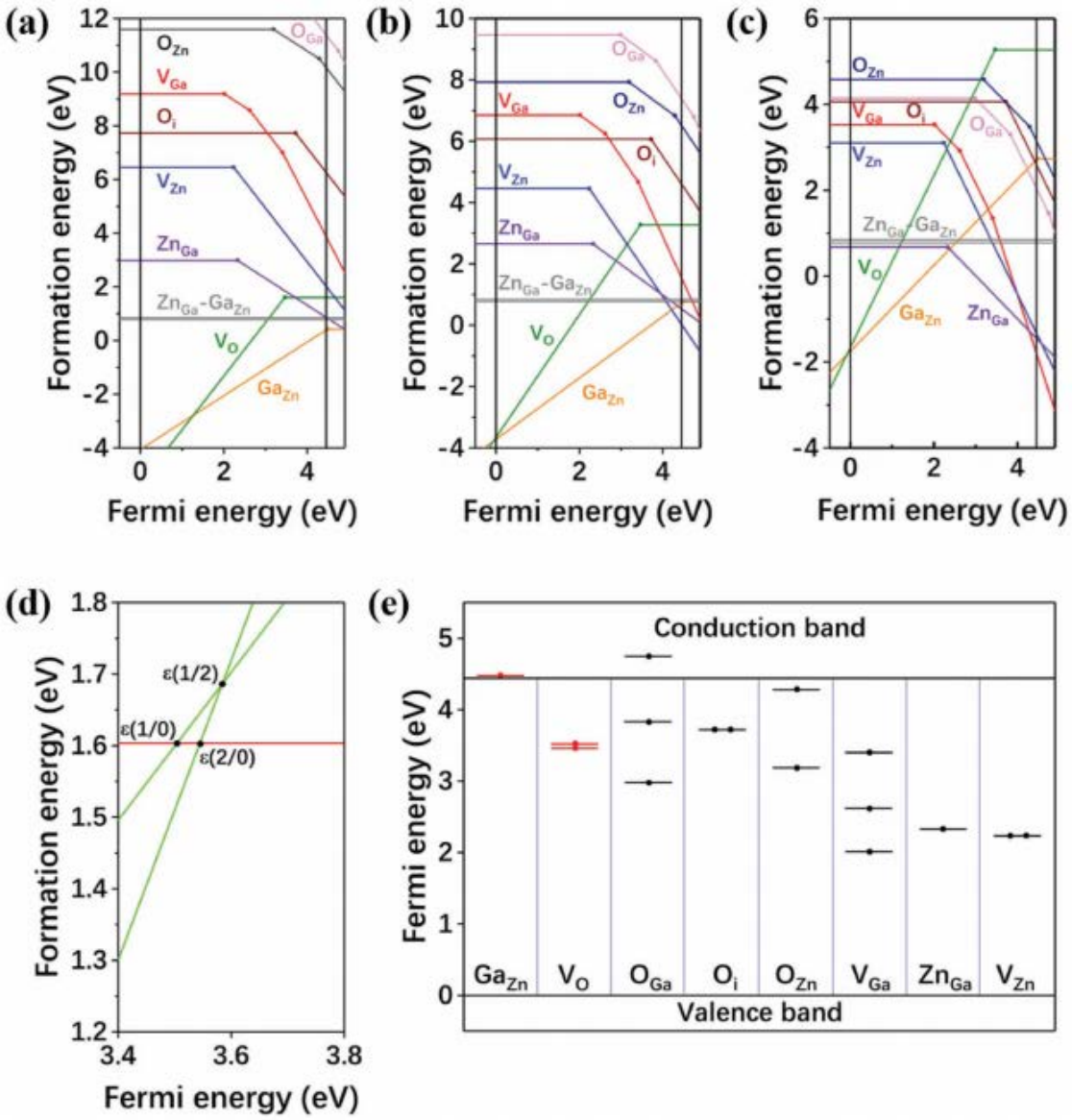

Figure 6. Theoretical calculations of defect levels. a–c) Calculated formation energy of various defects as a function of the Fermi energy E_F. d) The formation energy of O vacancy with different charge states as a function of the Fermi energy E_F. e) Calculated transition energy levels for various defects.

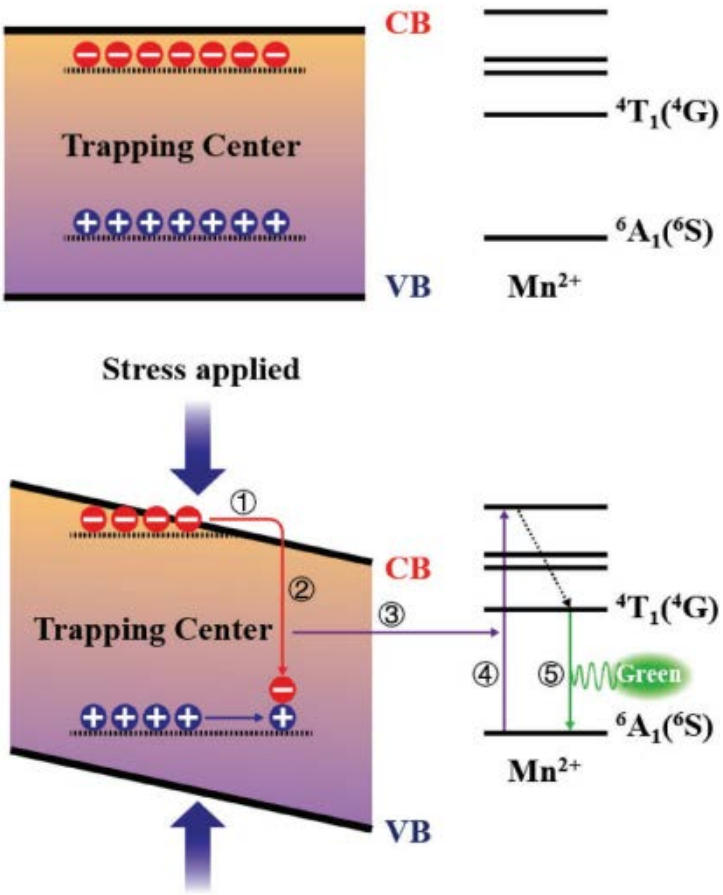

491

492 **Figure 7.** Illustration of the possible mechanism of pressure-induced luminescence.

Table 1. Physical parameters of various material systems used for temperature sensing.

System	Temperature range [K]	Racah parameter B [cm^{-1}]	β [cm^{-1}]	Crystal size [nm]	Relative sensitivity [$\%K^{-1}$] (temperature, K)	Ref.
Cr^{3+}:Ga_2O_3 GC	298–563	739	0.8050	2–5	0.46 (370)	[29]
Cr^{3+}:$ZnGa_2O_4$ GC	298–563	648	0.7058	5–8	0.58 (420)	[29]
Yb^{3+}/Er^{3+}/Cr^{3+}: YF^{3+}/Ga_2O_3 GC	303–563	723	0.7875	8	0.59 (386)	[30]
Cr^{3+}:$LiGa_5O_8$ GC	293–563	733	0.7984	8–15	0.76 (295)	[30]
Cr^{3+}:$LiAl_5O_8$	20–670	737	0.8028	–	0.83 (447)	[31]
Cr^{3+}:$LiGa_5O_8$ GC	293–563	729	0.7941	–	1.15 (350)	[32]
Mn^{2+}:Zn_2SiO_4	303–573	–	–	–	1.65 (573)	[33]
Mn^{2+}:$ZnGa_2O_4$ NG	323–523	740	0.7708	40[a)]	2.51 (523)	This work

[a)]Calculated from X-ray diffraction.